Progress In Electromagnetics Research M, Vol. 79, 113–126, 2019

CSAR Imaging of Electromagnetically Coupled Conducting Scatterers

Nicolas A. Guido, Evan T. Hiatt, and Enson Chang*

Abstract—Chipless RFID with small, printed metal tags have been proposed as a cost-effective alternative to chip-based technologies. A potentially viable configuration is to image the patches of different shapes, sizes, and orientations within a tag with a tabletop-scale synthetic aperture radar (SAR), operating in the V or W band. Information is encoded into, e.g., polarization, resonance characteristics, and phase of the scattered signal. The effect of electromagnetic coupling and sidelobe interference between closely spaced metal patches on SAR image has not been addressed in prior studies. To be specific, we analyze 60 GHz circular SAR (CSAR) imagery of subwavelength patches separated by distances on the order of wavelength. The scattered field is calculated with the method of moments (MoM) to account for EM interaction. The field is then used to form CSAR image with the polar formatting algorithm (PFA). Significant distortion of the CSAR image is found at this scale. Sidelobe interference causes image distortion and up to 7 dB of intensity modulation with patch separation. EM coupling produces an "interaction image," an artifact that extends between the patches. The source of this effect is traced to induced currents and charges residing on the patches' inner edges. Increasing system bandwidth or changing the incidence angle has minimal effect on both classes of image artifacts, highlighting the importance of accounting for them in practical system design and subsequent information processing.

1. INTRODUCTION

Automotive and UAV applications are fueling the development of short-range millimeter wave radars in 24–80 GHz range [1–3]. Synergy between these radars and 5G telecommunication technologies will undoubtedly lead to higher bandwidth, lower cost, and potential adoption in chipless Radio Frequency Identification (RFID), wearable technology, or Internet of Things (IoT). This paper focuses on chipless RFID using a radar to read small, printed metal patches in an RFID tag, as described by several U.S. patents [4–6]. References [4] and [6], for example, envision using polarization, resonance characteristics, and signal phase to embed a dense set of information within multiple conducting patches in a tag. Making such concepts viable involves interesting signal processing challenges.

Printing cost considerations require the patches to be closely packed within a space comparable to V- or W-band signal wavelength, implying a radar aperture comparable to the several meter readout range. Synthetic aperture radar (SAR) [7–9] can achieve such a large aperture at reasonable cost. A variety of SAR configurations may be appropriate for chipless RFID, including SAR or inverse SAR (ISAR) in both linear and rotational geometries. A recent paper, for example, examines stripmap SAR performance with MIMO sparse array [10]. The interaction between closely spaced conducting elements, however, has not been addressed. This study analyzes the sidelobe interference and electromagnetic (EM) coupling between conducting patches under circular SAR (CSAR) imaging [11].

Received 2 September 2018, Accepted 10 February 2019, Scheduled 7 March 2019
* Corresponding author: Enson Chang (echang@apu.edu).
The authors are with the Department of Mathematics, Physics, and Statistics, Azusa Pacific University, USA.

Unlike stripmap or spotlight SAR which requires bandwidth to achieve high range resolution, CSAR can produce bandwidth-independent subwavelength resolution in two dimensions. CSAR also has favorable speckle suppression properties [12] and allows imaging in 3D [11, 13]. Although the main lobe width of CSAR's point response is $\lambda/4$, the response has an extended circular sidelobe structure. Sidelobes of nearby scatterers interfere with each other to produce image artifacts. In addition, EM scattering is affected by nearby conductors, a coupling effect that becomes important when conductor separation is on the order of signal wavelength. The extent to which these effects can be mitigated will limit the achievable tag element density.

An alternative subwavelength imaging method with desirable sidelobe properties is Time Reversal imaging with Multiple Signal Classification (TR-MUSIC) [14]. TR-MUSIC leverages eigenspace decomposition used in the traditional MUSIC algorithm [15, 16] for super-resolution. Its performance has been carefully analyzed in [17–19]. By using multiple transmitters and receivers simultaneously, TR-MUSIC has intrinsically higher spatial diversity than the single transceiver SAR. In a full-aspect configuration with sensors surrounding the target area, TR-MUSIC is expected to have better sidelobe properties than CSAR.

There are practical tradeoffs between TR-MUSIC and CSAR. TR-MUSIC's resolvable degrees of freedom is the lesser of the number of transmitters or receivers [14, 20], which dictates the rank of the multistatic data matrix (MDM), the central quantity that embodies the scene information. An RFID tag that contains a large quantity of information will require many sensors, even in the absence of clutter. CSAR minimizes cost with a single transceiver, albeit at the expense of increased mechanical complexity and elevated sidelobe levels. Since cost is the primary driver toward chipless RFID, it inevitably impacts algorithm selection. As discussed in Section 4, a hybrid method that combines CSAR with TR-MUSIC should be considered in the future.

This paper analyzes CSAR imaging of conducting patches via simulation. We use Matlab's Method of Moments (MoM) tool to calculate induced currents, charges, and scattered electromagnetic field at the radar [21–23]. A CSAR processor with the polar-formatting algorithm (PFA) [8] then produced images of two adjacent square conducting patches. These images are analyzed to delineate the effects of sidelobes and EM coupling. Both effects are found significant in the regime of interest to chipless RFID.

Section 2 of this paper describes the system configuration and simulation procedure, including the MoM calculation, CSAR simulation, and the method for separating sidelobe interference from EM coupling. Section 3 describes simulation results. Section 4 summarizes the results, discusses potential mitigation approaches and future work. For completeness, an appendix outlines the CSAR imaging algorithm and its point response.

Notation Bold Latin letters, e.g., $\mathbf{A}$, $\mathbf{J}$, $\mathbf{E}$, represent three-dimensional vectors. Superscript, e.g., $\mathbf{E}^s$, $\mathbf{E}^i$, represents scattered or incident field. Subscript, e.g., $\mathbf{E}_{\tan}$, denotes vector component. Bold Greek letters, e.g., $\boldsymbol{\kappa}$, represents two-dimensional vectors in the x-y plane. Unit vectors are denoted with caret, e.g., $\hat{\phi}$ Estimated scalar quantities use plain font with caret, e.g., $\hat{\eta}$. Complex conjugate is denoted by *. Primed coordinates, e.g., (x', y', z'), denote target location in the target-fixed reference frame.

2. SIMULATION PROCEDURE

2.1. Chipless RFID Simulation Configuration

The CSAR system comprises a monostatic pair of radar transmitter and receiver, directed at a rotating area containing the RFID tag in an inverse SAR (ISAR) configuration. This configuration is mechanically less complex and has the advantage that clutter from the fixed background is strongly suppressed by CSAR's Doppler-dependent matched filter. For analysis purposes, however, it is more natural to model the problem in the target-fixed coordinate system with the origin at the center of the rotating platform, as shown in Fig. 1. A scatterer's location is denoted by $\mathbf{r}' = (x', y', z')$ with $z' = 0$. The radar rotates about the targets in this reference frame with polar angle θ, azimuthal angle ϕ, and distance R to the origin. The distance between a scatterer and the radar is $r = \sqrt{(R_h \cos\phi - x')^2 + (R_h \sin\phi - y')^2 + (R\cos\phi - z')^2}$, where R_h is the radius of the radar's

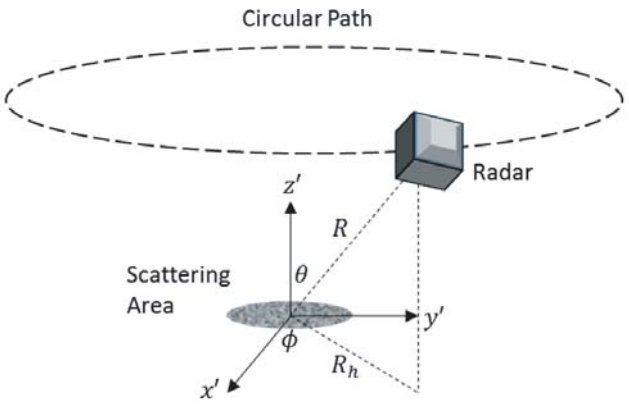

Figure 1. Simulation configuration in the target-fixed frame with radar at (R, θ, ϕ) and rotating about the z' axis. Target location is denoted by (x', y', z') with $z' = 0$.

horizontal projection in the x'-y' plane.

An FMCW radar mixes the received signal with a reference chirp over the sweep period. Neglecting multiple scattering and spherical spreading, the dechirped signal is:

$$s(t, \phi) = \left[\int dx' dy' \eta(x', y') \, g\left(t - \frac{2r}{c}\right) \right] g^*(t), \tag{1}$$

where t denotes the radar fast time, and ϕ is the radar's azimuthal angle. The expression in $[\cdot]$ is the backscattered signal under the Born approximation, where $\eta(x', y')$ is the scattering amplitude at (x', y'), $g(t)$ is the transmitted waveform, c is the speed of electromagnetic waves, and $2r/c$ represents the two-way signal delay. The mixing operation that multiplies the scattered signal with the complex conjugate of the transmitted signal reduces signal frequency to the audio band for ease of data acquisition. Instead of range compressing at this stage, CSAR accomplishes both range and azimuth compression with a 2D matched filter on the dechirped data, as described in Section 2.3 and the Appendix.

The transmitted FMCW waveform is

$$g(t) = e^{i2\pi(f_0 + \alpha t)t}, \tag{2}$$

where f_0 is the center frequency, $\alpha = B/2T$ is the sweep parameter with bandwidth B and sweep time T. To be specific, the baseline model in this paper uses $f_0 = 60\,\text{GHz}$, $B = 2\,\text{GHz}$, and $T = 10\,\text{msec}$.

Combining Eqs. (1) and (2) and neglecting the term proportional to r^2/c^2 in the exponent gives

$$s(t, \phi) = \int dx' dy' \eta(x', y') \, e^{-i2\pi(f_0 + 2\alpha t)\frac{2r}{c}} = \int dx' dy' \eta(x', y') \, e^{-i4\pi f \frac{r}{c}}, \tag{3}$$

where $f = f_0 + 2\alpha t$ is the instantaneous frequency at t. Given this one-to-one correspondence between f and t, the dechirped signal will be referred to as $s(f, \phi)$ throughout the rest of this paper. Equation (3) serves as the starting point of the CSAR processor outlined in the Appendix. While the processor makes the single-scattering assumption, $s(f, \phi)$ is calculated with a full-fidelity simulation, as described in the next section.

2.2. Signal Simulation

Figure 2 shows the basic target configuration with two square perfect electrical conductor (PEC) patches aligned along the x' axis, centered at the origin. The size of each patch is 3.2 mm (1/8″), or 0.64λ, where $\lambda = 5\,\text{mm}$ is the wavelength at 60 GHz. The center-to-center separation between the patches, d, varies from 0.64λ to 3.2λ (3.2 mm to 16 mm). For reference, the signal wavelength at 60 GHz is also shown in Fig. 2. Since the patch size and separation are comparable to wavelength, high order multiple scattering is to be expected.

The induced currents and charges that constitute re-radiation sources migrate with incident direction in a conductor, contrary to the standard SAR imaging assumption that $\eta(x', y')$ is independent

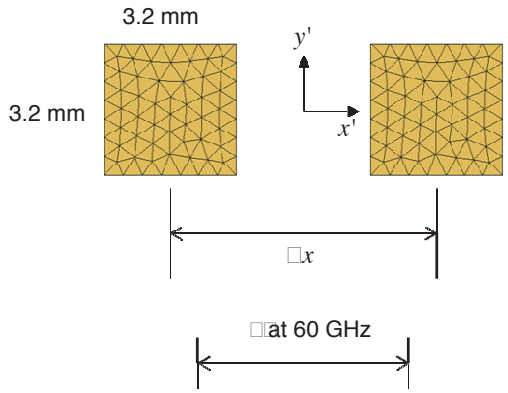

Figure 2. Two conducting, 3.2 mm square patches in the basic simulation configuration. The patch size and separation are both on the order of the signal wavelength at 60 GHz. MAT divides each patch into a triangular mesh for MoM computation.

of radar direction. The complex field-conductor interaction is modeled with an MoM approach in Matlab's Antenna Toolbox (MAT). Unlike finite difference or finite element methods, MoM does not require a 3D computational domain that tends to have residual boundary effects [24]. For PEC targets, MoM only calculates current and charge distributions over the 2D conductor surface. The resulting time saving is important for this study, which simulates scattering from many directions over a large parameter space. The current and charge distributions naturally produced by MoM are also useful for interpreting CSAR image — it is after all these sources that CSAR images. Alternatively, a multiple scattering approach [25] which systematically incorporates higher order scattering into the CSAR processor may improve performance in the future. This paper uses MoM as it is already efficiently implemented in MAT.

MAT divides each patch into a triangular mesh of elements. The Rao-Wilton-Glisson basis [22, 23] over these elements is used to solve an electric field integral equation (EFIE) for the current distribution on the conductors [26]. The EFIE comes directly from Maxwell's equations by applying the conducting boundary condition. The description below summarizes the basic set of equations pertinent to EFIE, as given in Section II of [22].

The scattered electric field from a time-harmonic incident wave of frequency f is

$$\mathbf{E}^s = -i2\pi f\mathbf{A} - \nabla\Phi, \tag{4}$$

where $\mathbf{A}$ and Φ are the magnetic vector potential and scalar electric potential, respectively. These potentials are due to the current density, $\mathbf{J}$, and surface charge density, σ, propagated from source points on the conductor to the field point at the radar by the free-space Green's function:

$$\mathbf{A} = \frac{\mu_0}{4\pi}\int_{S'}\mathbf{J}\frac{e^{-i2\pi f\frac{r}{c}}}{r}dS', \quad \Phi = \frac{1}{4\pi\epsilon_0}\int_{S'}\sigma\frac{e^{-i2\pi f\frac{r}{c}}}{r}dS'. \tag{5}$$

In the above equations, S' denotes the conductor surface, and r is the distance from the source point to the radar. The surface charge density and current density satisfy the continuity equation

$$\nabla\cdot\mathbf{J} = i2\pi f\sigma. \tag{6}$$

On the surface of the conductor, the tangential component of the incident electric field satisfies the EFIE:

$$\mathbf{E}^i_{\tan} = i2\pi f\mathbf{A} + \nabla\Phi. \tag{7}$$

Equation (7) must be solved consistently with Eqs. (5) and (6) over S'. The primary output of the calculation is the current distribution $\mathbf{J}$, which spans over the mesh elements with a basis set described in Section II of [22]. Reference [23] (Appendix B) provides additional details on the exact forms of integral solutions, including the self-contribution within a mesh element. We are interested in the scattered field from Eq. (4) for CSAR image formation and the current/charge distributions, $\mathbf{J}$ and σ, for CSAR image interpretation.

The combination of Eqs. (4) and (5) can be considered a more exact form of the backscattered signal in Eq. (1). The radar signal $s(f,\phi)$ is the component of the electric field along the receiver antenna. To be specific, this paper considers horizontally polarized incident and received fields, i.e., HH polarimetric configuration. In terms of spherical coordinates, both transmission and reception involve the electric field component in the $\hat{\phi}$ direction, where $\hat{\phi}$ is the unit vector in the direction of increasing ϕ. Despite this specific choice, the conclusions below regarding the significance of sidelobes and EM coupling apply equally well to other polarimetric combinations.

The received signal, $s(f,\phi)$, is computed over a discrete grid. In our simulation regime, $s(f,\phi)$'s frequency dependence is dominated by the two-way propagation phase factor, $e^{-2i(\frac{2\pi f}{c})r}$. It is verified numerically that the quantity $s(f,\phi)e^{2i(\frac{2\pi f}{c})R}$, where R is the distance from the radar to the target origin, is essentially independent of frequency over the 59 to 61 GHz band. The simulations below compute $s(f,\phi)e^{2i(\frac{2\pi f}{c})R}$ at 60 kHz.

The azimuthal grid spacing of $s(f,\phi)$ must satisfy the Doppler sampling criterion implied by the phase factor in Eq. (3), i.e., $4\pi(f/c)(r_{\max}{}'\Delta\phi) \leq \pi$, where $\Delta\phi$ is the angular increment between FMCW sweeps, $r_{\max}{}'$ is the maximum target radial extent, and $r_{\max}{}'\Delta\phi$ is the maximum possible radial movement of a scatterer between consecutive sweeps. The simulations below use $\Delta\phi = 2^\circ$, corresponding to a $r_{\max}{}'$ of about 3.5 cm, which is considerably larger than the actual target extent. At each angle, the scattered electric field calculation assumes that the radar is stationary during transmission and reception, consistent with the standard stop-and-hop approximation in SAR simulations.

2.3. CSAR Processing

CSAR imaging for the general geometry is described in detail in [11–13]. When $r_{\max}{}' \ll R$, the procedure is greatly simplified by inverting Eq. (3) for the scattering amplitude, $\eta(x',y')$, with a 2D Fourier transform, as outlined in the Appendix (Eqs. (A1)–(A5)). The key step that enables 2D FFT is an interpolation from polar to rectangular coordinates, known as the polar formatting algorithm (PFA). An excellent source of SAR operation principle and algorithms is [7]. More specifically, PFA is described in Section 10.3 of this reference and in more detail in Section 3.3 of [8].

The resultant scattering amplitude estimate, $\hat{\eta}$, from the Appendix is

$$\hat{\eta}\left(x',y'\right) = \int s\left(f,\phi\right) e^{ikR} e^{-i(\kappa_x x' + \kappa_y y')} \frac{d\kappa_x d\kappa_y}{\left(2\pi\right)^2}, \tag{8}$$

where frequency and wavenumber are related in the following manner:

$$k \equiv \frac{4\pi f}{c}, \tag{9}$$

$$\kappa_x = k\frac{R_h}{R}\cos\phi, \quad \kappa_y = k\frac{R_h}{R}\sin\phi. \tag{10}$$

The caret over η is a reminder that $\hat{\eta}$ is a bandlimited estimate of the actual η. The domain of $s(f,\phi)$, or equivalently, $s(\kappa,\phi)$, is an annular region bounded by the values of κ corresponding to the system's minimum and maximum frequencies. (See Eqs. (9) and (10).) Following the standard PFA procedure, $s(f,\phi)$ is interpolated onto a uniform rectangular grid in κ_x, κ_y, which then allows the use of 2D FFT to calculate $\hat{\eta}$. The simulations below use 4096 FFT in κ_x and κ_y with Nyquist value of $1.26\times10^4\,\mathrm{m}^{-1}$, corresponding to a square pixel size of $\Delta x' = \Delta y' = 0.25$ mm in the image domain.

2.4. Separating Sidelobe Interference from EM Coupling

Since CSAR imaging is linear, sidelobe interference and EM coupling can be separately in the following way:

1) Simulate the "total" field $\hat{\eta}_{total}$ with both patches present. This field contains both sidelobe interference and EM coupling.

2) Simulate the individual fields $\hat{\eta}_1$ and $\hat{\eta}_2$ of each patch by itself and add the results to form the "sum" field $\hat{\eta}_{sum} = \hat{\eta}_1 + \hat{\eta}_2$. This field contains sidelobe interference but not EM coupling.

3) Find the difference $\hat{\eta}_{EM} = \hat{\eta}_{total} - \hat{\eta}_{sum}$, which is due to EM coupling alone.

Similarly, linearity of Maxwell's equations allows the same decomposition to isolate currents and charges due to EM coupling. MAT is used below to derive the total, sum, and difference currents and charges. The difference **J** and σ are solely due to EM coupling and responsible for $\hat{\eta}_{EM}$.

3. SIMULATION RESULTS

3.1. CSAR Images of Individual and Multiple Conducting Patches

In Sections 3.1–3.3 we assume the radar to be in the same horizontal plane as the scattering area, i.e., $\theta = 90°$, and $R = R_h = 2\,\text{m}$. The result of other incidence angles is discussed in Section 3.4. To

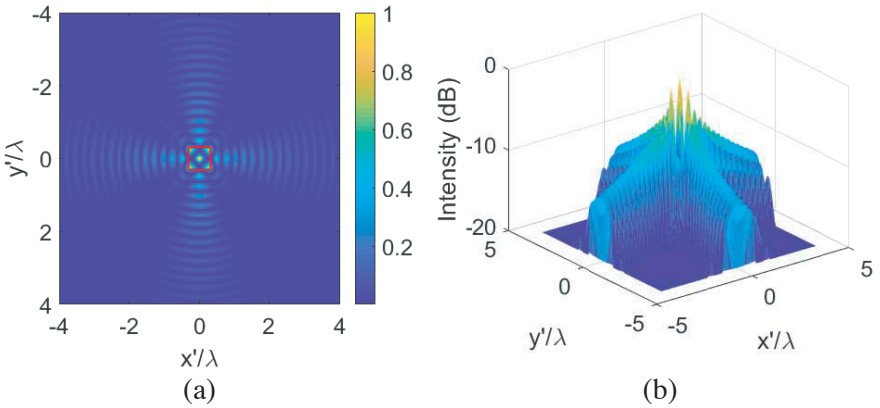

Figure 3. CSAR intensity image of a 0.64λ (3.2 mm) square patch: (a) on a linear scale with the red box marking the boundary of the square patch, and (b) on a dB scale, showing the collection of highlights in the patch and slowly decreasing sidelobes.

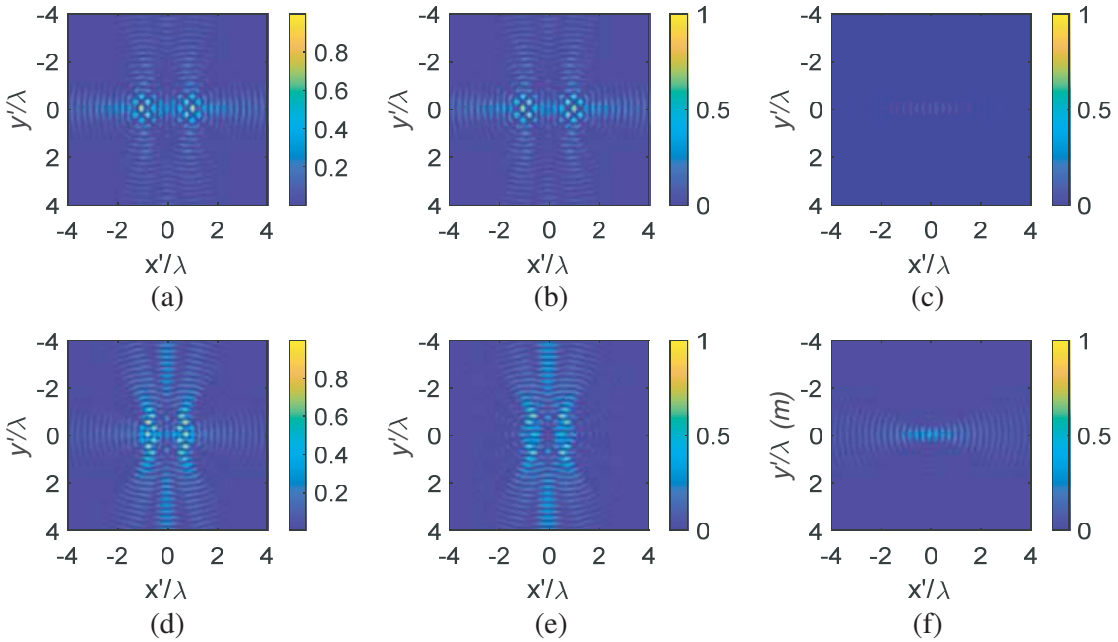

Figure 4. The total, sum, and difference images of two patches. (a)–(c) Total, sum, and difference images for center-to-center separation of $d = 1.9\lambda$ (9.6 mm); (d)–(f) Same set of images with $d = 1.3\lambda$ (6.4 mm).

illustrate the sidelobe structure, the CSAR intensity image, $|\hat{\eta}(x', y')|^2$, of a single 0.64λ (3.2 mm) patch centered at the origin is shown in Fig. 3(a) on a linear intensity scale. All distances are labeled in units of λ. The red box marks the physical boundary of the patch. Instead of a uniformly illuminated square, the patch appears to be a collection of highlights at $\lambda/4$, or 1.25 mm spacing. This grid of highlights is an interference pattern produced by the sub-aperture images that make up the full circular aperture.

Figure 3(b) shows the 3D surface plot of the intensity field on a dB scale. Sidelobes extend into an area many times the actual patch size. Those sidelobes immediately outside the patch boundary is 3 dB lower than the central peak, whereas sidelobes 4λ away only decrease by another 9 dB, illustrating the persistence of these sidelobes.

Figures 4(a)–(c) show the total, sum, and difference images of two patches separated by a relatively large distance of $d = 1.9\lambda$ (9.6 mm, measured center to center). All three images are normalized by the maximum intensity of the total image. The total and sum images in Figs. 4(a) and 4(b) are nearly identical due to negligible EM coupling at this separation. Figs. 4(d)–(f) show the same set of three images for two patches separated by $d = 1.3\lambda$ (6.4 mm), also normalized by the maximum intensity of the total image. Sidelobe interference is significant at this separation. Although the total and sum images in this case have similar structure and overall intensity, there are noticeable differences between them due to EM coupling. The EM coupling image in Fig. 4(f) extends along the line connecting the patches. Its maximum intensity is 58% that of the total image and primarily occupies the region between patch centers.

3.2. Sidelobe Interference

Besides the image distortion seen in Figs. 4(d) and 4(e), sidelobe interference also causes significant variation in the overall image intensity. Figs. 5(a)–(c), all normalized to the maximum intensity of 5(c), illustrate this effect for a patch separation of 1.0λ (5 mm). Figs. 5(a) and 5(b) show the individual patch images. Fig. 5(c) is the sum image, the maximum intensity of which is 230% that of the individual

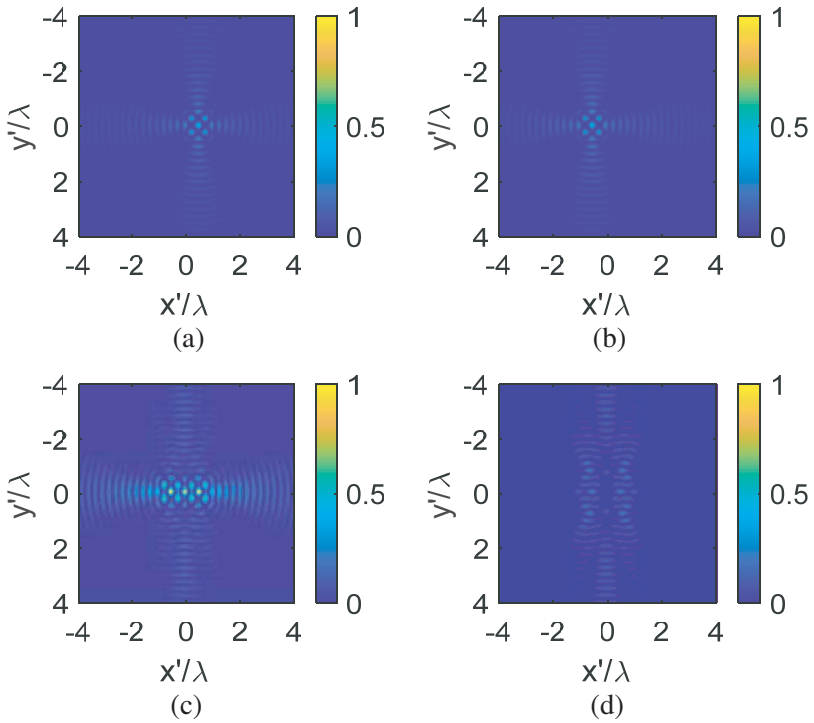

Figure 5. Image sidelobes can interfere constructively or destructively. (a) and (b) are images of two individual patches separated by $d = 1.0\lambda$ (5 mm). (c) The sum image showing higher intensity than either individual image. Contrasting this with (d) the sum image with $d = 1.26\lambda$ (6.3 mm), showing destructive interference.

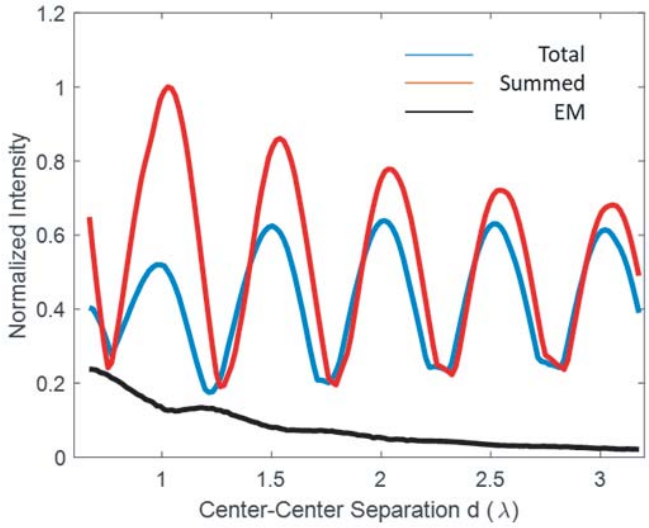

Figure 6. Dependence of the image intensity on patch separation, d. The total, sum, and EM curves are in blue, red, and black, respectively.

patches, indicating constructive interference. In contrast, Fig. 5(d) illustrates the sum image with 1.26λ (6.3 mm) patch separation, also normalized the same way. Its maximum intensity is only 44% that of the individual images, indicating destructive interference.

Figure 6 depicts the full dependence of image intensity on patch separation, d. The red curve, normalized to unit peak value, represents the maximum intensity of the sum image. It shows a clear interference effect with $\lambda/2$ (2.5 mm) period, which agrees with the period of the CSAR amplitude response in Eq. (A6) (not to be confused with the $\lambda/4$ periodicity of the *intensity* response). There is a 7 dB difference between the maximum near $d = 1.0\lambda$ (5 mm) and minimum near $d = 1.26\lambda$ (6.3 mm). This strong intensity dependence on patch spacing suggests care must be taken in chipless RFID design to avoid destructive interference.

A variety of sidelobe suppression techniques are useful for traditional radar imaging, including spectral windowing, nonlinear techniques such as spatially variant apodization (SVA [27, 28]), and SVA's extensions for spectral extrapolation (Super-SVA [29], Adaptive Sidelobe Reduction [30]). The effectiveness of such techniques for CSAR imaging in the subwavelength regime is questionable. Unlike fully sampled radar data, $s(f, \phi)$ occupies a thin annular region in the $f - \phi$ domain, extending from 59 to 61 GHz. The "sidelobes" with $\lambda/4$ spacing are more properly considered grating lobes or ambiguities due to the missing data from DC to 59 GHz. Windowing and SVA (which nonlinearly combines windows) are not effective against grating lobes. The utility of spectral extrapolation techniques operating over such a wide domain is also dubious. Two other options, image deconvolution and TR-MUSIC, are discussed in Section 4 as future work. Increasing bandwidth can reduce the more distant sidelobes, as discussed in Section 3.4.

3.3. Electromagnetic Coupling

The extent of EM coupling is shown as the black curve in Fig. 6. It is the maximum intensity of the difference image as a function of patch separation. This curve comes close to the intensity of the sum image (red curve) near $d = 0.7\lambda$ and 1.2λ, where the sum is near destructive interference. EM coupling generally decreases with patch separation, although there are several mild resonances. The blue curve in Fig. 6 corresponds to the peak intensity of the total image, including the effect of both sidelobe interference and EM coupling. EM coupling tends to offset the interference effect such that the total image intensity is weaker than the sum image in general. This effect is most noticeable at small patch separations where EM coupling is strong. The total image's first peak near $d = 1\lambda$ is actually weaker than its second peak near 1.5λ.

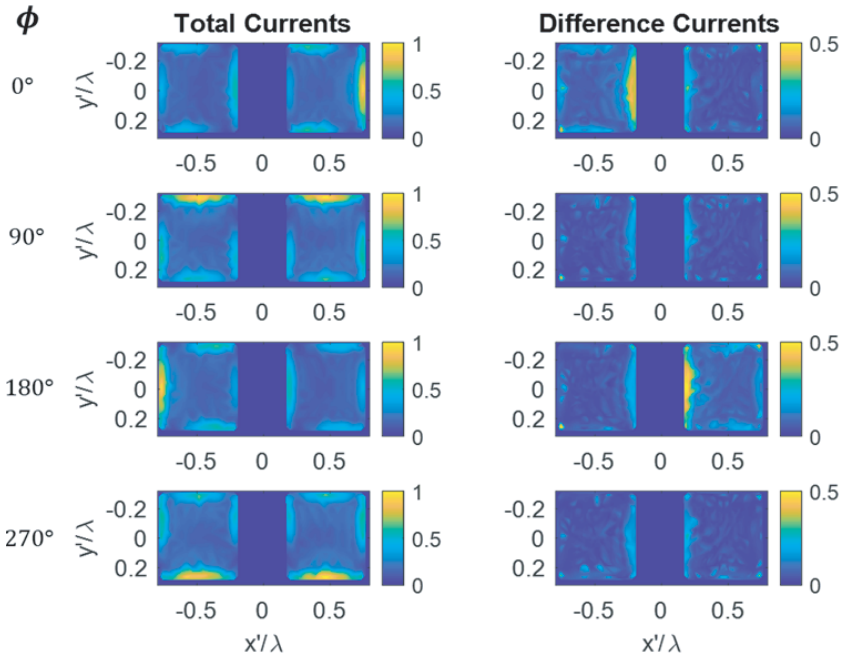

Figure 7. Induced currents in the two patches at four radar angles, $\phi = 0°, 90°, 180°, 270°$. The left column is the total current distribution. The right column is the difference current distribution due to EM coupling.

The opposing effects of sidelobe interference and EM coupling as well as the morphology of the EM-coupling image in Fig. 4(f) can be explained by the distribution of induced currents and charges. The magnitude of the induced currents for four radar angles are shown in the left column of Fig. 7 for two patches separated by λ. At $\phi = 0°$, the induced currents concentrate around the right edge of the patches toward the radar direction. The maximum current in the right patch is considerably stronger than that in the left one, an asymmetry due to EM coupling. The situation reverses when $\phi = 180°$. At $\phi = 90°$ and $270°$, the induced currents concentrate along the patches' top or bottom edges with identical magnitudes since the patches are equally illuminated by the radar. Although not shown, the same calculations for each patch by itself shows equal currents at the four angles by symmetry.

Following the procedure described in Section 2.4, we calculate the "sum" currents by superposing the two single-patch currents. The difference between the total and sum currents represents the change due to EM coupling, which is shown in the right column of Fig. 7. (Note the color scale change in the right column.) At $\phi = 0°$ the difference currents reside on the inner edge of the left patch; they shift to the inner edge of the right patch when $\phi = 180°$. The difference currents at 90° and 270° are much weaker by comparison. EM coupling-induced charges (not shown) behave in a similar way, also residing along the inner edges of the patches and reaching their maximum density at $\phi = 0°$ or 180°.

Since the difference currents and charges are only active near 0° and 180°, the difference EM field is only significant near these angles. The resultant image is an elongated feature along those directions, the length of which is governed by the 7.5 cm range resolution corresponding to 2 GHz bandwidth (viz. $\delta_r = c/2B$ where δ_r is range resolution). The actual extent of the horizontal image feature in Fig. 4(f) is shorter than 7.5 cm due to integration over a finite angular extent around 0° and 180°, affording some degree of "smearing" of the range response over angle. The range responses of the two patches add such that the interference pattern has maximum intensity between the patch centers, as seen in Fig. 4(f).

Regarding the opposing effects of sidelobe interference and EM coupling, note that sidelobe interference is most prominent when the two patches have equally intense sidelobes. EM coupling, however, causes asymmetrical distribution of currents and charges in the two patches, reducing the magnitude of sidelobe interference.

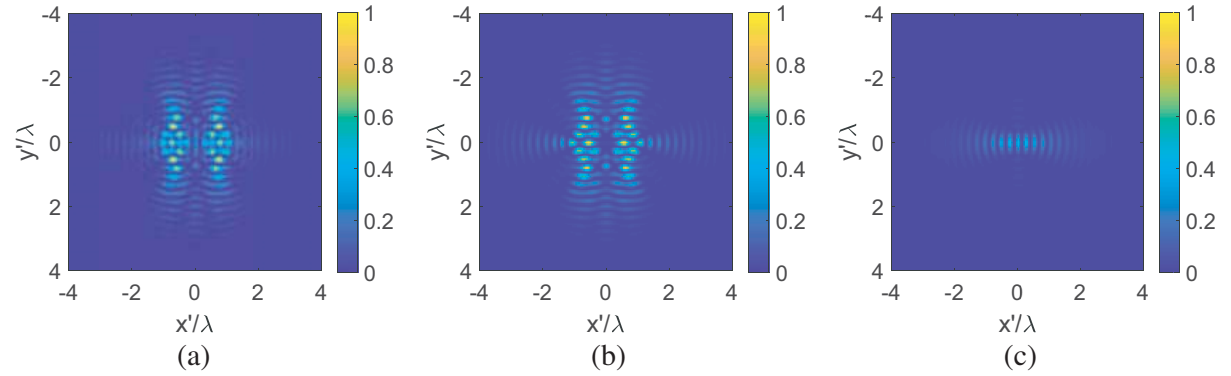

Figure 8. The total, sum, and difference images of two patches separated by 1.3λ (6.4 mm). The system frequency is from 55 to 65 GHz. (a) total image, (b) sum image, and (c) difference image.

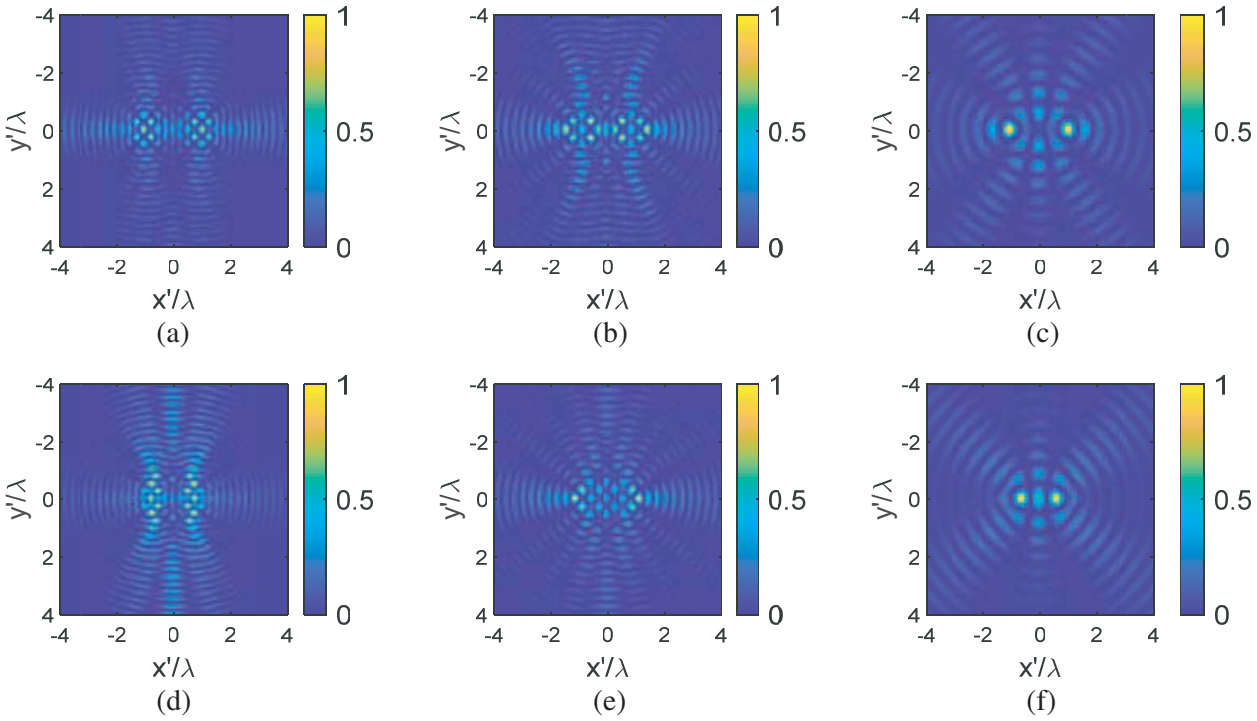

Figure 9. Incidence angle dependence of CSAR (total) images of two patches separated by 1.9λ (9.6 mm) in (a)–(c), and 1.3λ (6.4 mm) in (d)–(f). For each patch separation, images are simulated for three different incidence angles, $\theta = 90°, 60°, 30°$ (corresponding to 0°, 30°, and 60° grazing).

3.4. Effect of Bandwidth and Incidence Angle

System bandwidth determines radar range resolution. Since the CSAR image can be thought of as the sum of sub-aperture images, each with its own range sidelobe along its look direction, one might expect increased bandwidth to mitigate CSAR sidelobes. This has only limited effectiveness in the subwavelength regime, however. The CSAR images of two patches separated by 1.3λ (6.4 mm) are simulated for a 55–65 GHz system. The slowly-varying function discussed in Section 2.2, $s(f,\phi)e^{2i(\frac{2\pi f}{c})R}$, is computed at 2 GHz intervals over the 10 GHz band and assumed to be piecewise linear in between.

Figure 8 shows the total, sum, and difference images. Comparing them with Figs. 4(d)–(f) shows that increasing bandwidth suppresses the more distant sidelobes. However, the first few orders of

sidelobes (which are more aptly described as grating lobes) remain persistent for the reason discussed in Section 3.2. It would take significantly larger bandwidth than 10 GHz to suppress these inner sidelobes, an unlikely prospect with current technology. The intensity of EM coupling image in Fig. 8(f) is similar to that in Fig. 4(f), indicating that bandwidth has little effect on EM coupling.

Incidence angle affects detailed image features as well as polarization-dependent scattering amplitude and the exact amount of EM coupling. However, the general characteristics of interference and coupling are not altered by incidence angle. Fig. 9 illustrates CSAR images at different incidence angles. Figs. 9(a)–(c) are the images of two patches with center-to-center separation $d = 1.9\lambda$ (9.6 mm) at three different incidence angles, $\theta = 90°, 60°, 30°$ ($0°, 30°$, and $60°$ grazing). Figs. 9(d)–(f) are the corresponding images for two patches separated at $d = 1.3\lambda$ (6.4 mm). For both patch separations, the images become less resolved with decreasing incidence angle (increasing grazing angle) due to radar range layover. The spatial diversity afforded by CSAR completely vanishes at $90°$ grazing, where all the scatterers are at nearly identical range. These results suggest that one should use grazing angles of order $30°$ or less for this application.

4. CONCLUSIONS

CSAR images of closely spaced conducting patches are distorted by sidelobe interference and EM coupling when patch size and separation are comparable to radar wavelength, a regime of interest to chipless RFID. Such image distortions can limit practically achievable patch density. This challenge is not unique to CSAR. In stripmap SAR, for example, the range response of patches closely packed in range can interfere, while EM coupling can cause both azimuthal and range artifacts.

Sidelobes of neighboring patches interfere to produce as much as 7 dB of image intensity variation with patch separation, at $\lambda/2$ periodicity. This result suggests the importance of judiciously chosen patch spacing in order to avoid destructive interference. The image of EM coupling-induced currents and charges concentrates along the line connecting the patches. The magnitude of this distortion decreases with patch separation, showing weak resonance peaks.

The "sidelobes" in CSAR images are actually grating lobes due to missing data from DC to the lower band edge. As such the sidelobes are resistant to conventional sidelobe suppression techniques and improved bandwidth. One candidate approach for mitigating such sidelobes is nonlinear image deconvolution such as CLEAN and WIPE [31, 32]. These algorithms have been employed in radio astronomy for removing severe grating lobes. As mentioned in the Introduction, TR-MUSIC has also demonstrated low sidelobe level in the subwavelength regime. Given CSAR's cost benefit and TR-MUSIC's desirable image quality, a hybrid method combining them, e.g., using several transceivers to cover subapertures in conjunction with a rotating target, may reap the benefits of both approaches.

Current CSAR formulation is based on the Born approximation with fixed scattering amplitude and location. The movement of induced currents and charges with radar direction in a conductor causes image smearing, manifested as interference patterns at the characteristic $\lambda/4$ spacing. The single-scattering TR-MUSIC faces the same issue. When scatterers vary, the eigenspectrum of the MDM does not cleanly separate into signal and noise subspaces, even in the absence of noise. (See e.g. [33].) The system's Green's functions are no longer strictly orthogonal to the noise subspace, the expected result of which is image distortion. A truly effective hybrid CSAR/TR-MUSIC algorithm should account for multiple scattering. Although this has been formulated in TR-MUSIC for a scalar field [34], vector field multiple scattering must be considered for radar imaging.

Future work will provide experimental verification of the simulated results, analyze consequences on RFID information processing, image deconvolution, as well as the prospect of a hybrid CSAR/TR-MUSIC setup.

APPENDIX A.

An overview of the CSAR processor is provided here for completeness. Eq. (3) is reproduced here as the starting point:

$$s\left(t,\phi\right) = s\left(f,\phi\right) = \int dx'dy'\eta\left(x',y'\right)e^{-i4\pi f\frac{r}{c}}, \tag{A1}$$

where $r = |\mathbf{R} - \mathbf{r}'|$ is the distance between the radar at $\mathbf{R} = (R_h \cos\phi R_h \sin\phi z)$ and a scatterer at $\mathbf{r}' = (x', y', 0)$. When $r' \ll R_h$, the distance r can be approximated by its linear expansion in r'/R:

$$s\left(f,\phi\right) \approx \int dx'dy'\eta\left(x',y'\right) e^{-i\frac{4\pi f}{c}\left(R-\frac{R_h}{R}\cos\phi x'-\frac{R_h}{R}\sin\phi y'\right)}. \tag{A2}$$

By making the following frequency-wavenumber associations

$$k = \frac{4\pi f}{c}, \quad \kappa_x = k\frac{R_h}{R}\cos\phi, \quad \kappa_y = k\frac{R_h}{R}\sin\phi, \tag{A3}$$

Eq. (A2) becomes

$$s\left(f,\phi\right) = \int dx'dy'\eta\left(x',y'\right) e^{-ikR}e^{i\kappa_x x'+i\kappa_y y'}. \tag{A4}$$

Although $s(f,\phi)$ is bandlimited, one can still formally invert the above equation to obtain an estimate of η:

$$\hat{\eta}\left(x',y'\right) = \int s\left(f,\phi\right) e^{ikR}e^{-i\kappa_x{}'x'-i\kappa_y{}'y'}\frac{d\kappa_x{}'d\kappa_y{}'}{\left(2\pi\right)^2}, \tag{A5}$$

namely that $\hat{\eta}(x', y')$ is the 2D Fourier transform of the received data multiplied by a frequency-dependent phase factor. The exponential factors in the integrand represent the 2D matched filter used by CSAR to accomplish simultaneous range and azimuth compression. The data $s(f,\phi)$ is computed on a regular grid within an annular region in the $f-\phi$ domain. Once it is interpolated onto a regular rectangular grid, 2D FFT can be used to do the integral in Eq. (A5) efficiently. This is the polar formatting algorithm.

For a unit point scatterer at the origin, i.e., $\eta(x', y') = \delta(x')\delta(y')$, the point response of an ideal system with flat spectrum over the frequency range $[f_{\min} f_{\max}]$ is

$$\begin{aligned}\hat{\eta}\left(x',y'\right) &= \int e^{-i\kappa_x x'-i\kappa_y y'}\frac{d\kappa_x d\kappa_y}{\left(2\pi\right)^2} \\ &= \frac{1}{2\pi r'}\left(\kappa_{\max}J_1\left(\kappa_{\max}r'\right) - \kappa_{\min}J_1\left(\kappa_{\min}r'\right)\right),\end{aligned} \tag{A6}$$

where $\kappa_{\min} = 4\pi f_{\min} R_h/(cR)$, and $\kappa_{\max} = 4\pi f_{\max} R_h/(cR)$, and r' is the radial distance of (x', y'). This is a circularly symmetric Airy pattern. Since $J_1(\rho) \sim \sqrt{\frac{2}{\pi x}}\cos(\rho - \frac{3\pi}{4})$ asymptotically, $\hat{\eta}$ has a radial period of approximately $2\pi/\kappa$, or $(R_h/R)(\lambda/2)$, where λ is the wavelength at the center frequency of the system. The intensity, $|\eta|^2$, has period $(R_h/R)(\lambda/4)$. The -3 dB width of the main lobe centered at the origin is also approximately $(R_h/R)(\lambda/4)$.

ACKNOWLEDGMENT

This work was supported in part by the 2018 California Space Grant Workforce Development Program through Azusa Pacific University's Center for Research in Science.

REFERENCES

1. Meinel, H. H., "Evolving automotive radar — From the very beginnings into the future," *Proc. EuCAP, The Hague*, Netherlands, 3107–3114, 2014.
2. Patole, S., M. Torlak, D. Wang, and M. Ali, "Automotive radars: A review of signal processing techniques," *IEEE Signal Proc. Mag.*, Vol. 34, No. 2, 22–35, Mar. 2017.
3. Felic, G. K., R. J. Evans, H. T. Duong, H. V. Le, J. Li, and E. Skafidas, "Single-chip millimeter wave radar," *Microwave J.*, Vol. 58, 108–116, Jan. 2015.
4. Pettus, M., "RFID system utilizing parametric reflective technology," U.S. Patent 7 460 016, Dec. 2, 2008.

5. Kofman, S., Y. Meerfeld, M. Sandler, S. Dukler, and V. Alchanatis, "Radio frequency identification system and data reading method," U.S. Patent 20090014520A1, Jan. 15, 2009.
6. Pettus, M., "RFID system utilizing parametric reradiated technology," U.S. Patent, 7 498 940, Mar. 3, 2009.
7. Curlander, J. C. and R. N. McDonough, *Synthetic Aperture Radar: Systems and Signal Processing*, John Wiley & Sons, Chichester, England, 1991.
8. Carrara, W. G., R. S. Goodman, and R. M. Majewski, *Spotlight Synthetic Aperture Radar Signal Processing Algorithms*, Artech House, Boston, MA, USA, 1995.
9. Chan, Y. K. and and V. C. Koo, "An introduction to Synthetic Aperture Radar (SAR)," *Progress In Electromagnetics Research B*, Vol. 2, 27–60, 2008.
10. Zomorrodi, M. and N. C. Karmakar, "Optimized MIMO-SAR technique for fast EM-Imaging of chipless RFID System," *IEEE Trans. Microw. Theory Techn.*, Vol. 60, No. 7, 2142–2151, Jul. 2012.
11. Soumekh, M., "Reconnaissance with slant plane circular SAR imaging," *IEEE Trans. Image Process.*, Vol. 5, No. 8, 1252–1265, Aug. 1996.
12. Musgrove, C., "Synthetic aperture radar speckle reduction for circle mode SAR images," *Proc. SPIE 9829, Radar Sensor Technology XX*, May 2016.
13. Ishimaru, A., T. Chan, and Y. Kuga, "An imaging technique using confocal circular synthetic aperture radar," *IEEE Trans. Geosci. Remote Sens.*, Vol. 36, No. 5, 1524–1530, Sep. 1998.
14. Devaney, A. J., "Time reversal imaging of obscured targets from multistatic data," *IEEE Trans. Antennas Propag.*, Vol. 53, No. 5, 1600–1610, May 2005.
15. Therrien, C. W., *Discrete Random Signals and Statistical Signal Processing*, Prentice Hall, New Jersey, 1992.
16. Stoica, P. and R. Moses, *Introduction to Spectral Analysis*, Prentice Hall, New Jersey, 1997.
17. Ciuonzo, D., G. Romano, and R. Solimenne, "Performance analysis of time-reversal MUSIC," *IEEE Trans. Signal Process.*, Vol. 63, No. 10, 2650–2662, May 2015.
18. Ciuonzo, D., "On time-reversal imaging by statistical testing," *IEEE Sig. Proc. Lett.*, Vol. 24, No. 7, 1024–1028, Jul. 2017.
19. Ciuonzo, P. and P. S. Rossi, "Noncolocated time-reversal MUSIC: High-SNR distribution of null spectrum," *IEEE Signal Process. Lett.*, Vol. 24, No. 4, 397–401, Apr. 2017.
20. Marengo, E. A., F. K. Gruber, and F. Simonetti, "Time-reversal MUSIC imaging of extended targets," *IEEE Trans. Image Process.*, Vol. 16, No. 8, 1967–1984, Aug. 2007.
21. Harrington, R. F., *Field Computation by Moment Methods*, Macmillan, New York, NY, USA, 1968.
22. Rao, S. M., D. R. Wilton, and A. W. Glisson, "Electromagnetic scattering by surfaces of arbitrary shape," *IEEE Trans. Antennas Propag.*, Vol. 30, No. 3, May 1982.
23. Wilton, D. R., S. M. Rao, and A. W. Glisson, "Electromagnetic scattering by arbitrary surfaces," Tech. Rep. RADC-TR-79-325, Rome Air Development Center, Griffiss AFB, NY, Mar. 1980.
24. Davidson, D., *Computational Electromagnetics for RF and Microwave Engineering*, Cambridge U. Press, Cambridge, 2005.
25. Twersky, V., "Multiple scattering of electromagnetic waves by arbitrary configurations," *J. of Mathematical Physics*, Vol. 8, No. 3, 589–610, Mar. 1967.
26. "Method of moments solver for metal structures," [Online], Available: https://www.mathworks.com/help/antenna/ug/method-of-moments.html.
27. Stankwitz, H. C., R. J. Dallaire, and J. R. Fienup, "Spatially variant apodization for sidelobe control in SAR imagery," *Proc. 1994 IEEE National Radar Conf.*, Mar. 1994.
28. Stankwitz, H. C., R. J. Dallaire, and J. R. Fienup, "Nonlinear apodization for sidelobe control in SAR imagery," *IEEE Trans. Aerosp. Electron. Syst.*, Vol. 31, No. 1, 267–279, Jan. 1995.
29. Stankwitz, H. C. and M. R. Kosek, "Sparse aperture fill for SAR using super-SVA," *Proc. 1996 IEEE National Radar Conf.*, May 1996.
30. DeGraaf, S. R., "Sidelobe reduction via adaptive FIR filtering in SAR imagery," *IEEE Trans. Image Process.*, Vol. 3, No. 3, 292–301, May 1994.

31. Högbom, J., "Aperture synthesis with a non-regular distribution of interferometer baselines," *Astrophys. J. Suppl. Ser.*, Vol. 15, 417–426, 1974.
32. Lannes, A., E. Anterrieu, and P. Marechal, "CLEAN and WIPE," *Astron. Astrophys. Suppl. Ser.*, Vol. 123, 183–198, May 1997.
33. Zhang, W., A. Hoorfar, and L. Li, "Through-the-wall target localization with time reversal MUSIC method," *Progress In Electromagnetics Research*, Vol. 106, 75–89, 2010.
34. Gruber, F. K., E. A. Marengo, and A. J. Devaney, "Time-reversal imaging with multiple signal classification considering multiple scattering between the targets," *J. Acoust. Soc. Am.*, Vol. 115, No. 6, 3042–3047, Jun. 2004.